

## Article

# Laser Cladding of a Ti–Zr–Mo–Ta–Nb–B Composite Coating on Ti60 Alloy to Improve Wear Resistance

Kaijin Huang <sup>1,2,\*</sup>  and Xianchao Han <sup>1</sup>
<sup>1</sup> State Key Laboratory of Materials Processing and Die & Mould Technology, Huazhong University of Science and Technology, Wuhan 430074, China; m202171092@hust.edu.cn

<sup>2</sup> Key Laboratory of Laser Technology and Optoelectronic Functional Materials of Hainan Province, Hainan Normal University, Haikou 571158, China

\* Correspondence: huangkaijin@hust.edu.cn; Tel.: +86-027-87543676

**Abstract:** To improve the wear resistance of the Ti60 alloy, laser cladding was used to obtain a composite coating containing a high-entropy  $(\text{Ti}_{0.2}\text{Zr}_{0.2}\text{Mo}_{0.2}\text{Ta}_{0.2}\text{Nb}_{0.2})\text{B}_2$  boride phase, with Ti, Zr, Mo, Ta, Nb, and B powders as the raw materials. The microstructure and wear characteristics of the coating were studied using XRD, SEM, EDS, and the pin-on-disc friction wear technique. The results show that the coating mainly consists of six phases:  $(\text{Ti}_{0.2}\text{Zr}_{0.2}\text{Mo}_{0.2}\text{Ta}_{0.2}\text{Nb}_{0.2})\text{B}_2$ ,  $\text{ZrB}_2$ ,  $\text{TiB}$ ,  $\text{TiZr}$ ,  $\text{Ti}_{1.83}\text{Zr}_{0.17}$ , and  $\text{Ti}_{0.67}\text{Zr}_{0.67}\text{Nb}_{0.67}$ . The average microhardness of the coating was  $1062.9 \text{ HV}_{0.1}$  due to the occurrence of the high-entropy, high-hardness  $(\text{Ti}_{0.2}\text{Zr}_{0.2}\text{Mo}_{0.2}\text{Ta}_{0.2}\text{Nb}_{0.2})\text{B}_2$  boride phase, which was about 2.9 times that of the Ti60 alloy substrate. The coating significantly improved the wear resistance of the Ti60 alloy substrate, and the mass wear rate was about 1/11 that of the Ti60 alloy substrate. The main types of wear affecting the coating were abrasive, adhesive, and oxidation wear, while the main wear affecting the Ti60 alloy matrix was abrasive wear, accompanied by a small amount of adhesive and oxidation wear.

**Keywords:** laser cladding; Ti60 alloy; high-entropy boride; wear resistance



**Citation:** Huang, K.; Han, X. Laser Cladding of a Ti–Zr–Mo–Ta–Nb–B Composite Coating on Ti60 Alloy to Improve Wear Resistance. *Coatings* **2024**, *14*, 1247. <https://doi.org/10.3390/coatings14101247>

Academic Editor: Rafael Comesaña

Received: 30 August 2024

Revised: 16 September 2024

Accepted: 23 September 2024

Published: 30 September 2024



**Copyright:** © 2024 by the authors. Licensee MDPI, Basel, Switzerland. This article is an open access article distributed under the terms and conditions of the Creative Commons Attribution (CC BY) license (<https://creativecommons.org/licenses/by/4.0/>).

## 1. Introduction

Ti60 titanium alloy is a nearly  $\alpha$ -type high-temperature titanium alloy that can be employed for long-term service even at a temperature of  $600^\circ\text{C}$ . As an important material used in aero-engine blades and compressors, it needs to withstand complex loads and high-friction and -wear conditions. For example, fretting wear will occur between the root of the rotor blade and the disc mortise due to the centrifugal force caused by the rotor blade rotating at high speeds or when the engine becomes overexcited. Due to vibrations, thermal expansion, and other factors during high-speed rotations, the blade tip will accidentally scrape the sealing coating on the inner wall of the casing, resulting in adhesive and abrasive wear. When the engine is used in an environment with desert dust or volcanic ash suspended at high altitudes, the hard particles in the air will impact the high-speed rotating blades, resulting in erosion wear. This highlights that the Ti60 titanium alloy also has some shortcomings, such as a low hardness ( $340 \text{ HV}$ ) [1] and insufficient friction and wear resistance; however, currently, no relevant studies have attempted to improve the wear resistance of Ti60 alloy.

However, many studies have reported the use of laser cladding technology to improve the wear resistance of other types of titanium alloys. For instance, Di et al. [2] prepared a high-entropy alloy coating of  $\text{AlCoCrFeMoVTi}$  on the surface of a TC4 titanium alloy via laser cladding technology. The experimental results show that the highest microhardness of the coating  $\text{HV}_{0.2}$  was  $10,990 \text{ MPa}$ , which was 3.29 times that of the substrate, and the wear volume of the coating was only 12.01% that of the substrate. Qin et al. [3] used laser cladding technology to prepare a  $\text{NiCrCoAlY-Cr}_3\text{C}_2$  composite coating on the surface of a TC4 titanium alloy. The results show that the highest microhardness of the composite

coating was 1344 HV, which was about 3.8 times that of the substrate (350 HV), and the wear loss of the coating was 24% that of the substrate. Jiang et al. [4] prepared a WC-Co composite coating using laser cladding to significantly improve the wear resistance of a TC4 substrate, making the maximum microhardness of the coating as high as 1536 HV<sub>0.5</sub> and the wear rate as high as 1.5 g/h. Huang et al. [5] used laser cladding technology to prepare a Ti<sub>5</sub>Si<sub>3</sub>/Ti<sub>3</sub>Al composite coating on a TA2 titanium alloy. The average microhardness of the coating was about 668 HV<sub>0.1</sub>, which was 3.34 times that of the matrix, and the mass wear rate of the coating was 1/5.79 that of the matrix. Yu et al. [6] used a semiconductor laser to laser clad a Ti-Ni-Si<sub>3</sub>N<sub>4</sub>-ZrO<sub>2</sub> mixed powder onto the surface of a TA15 alloy to prepare a ZrO<sub>2</sub>/Ti<sub>5</sub>Si<sub>3</sub>/TiN/Ti<sub>2</sub>N composite coating. The results show that the microhardness of the composite coating was 835–1050 HV, which was about three times that of the substrate. Under dry sliding friction and wear, the wear of the coating was about 1/6 that of the substrate. Feng et al. [7] used laser cladding technology to prepare a TiB-TiC co-reinforced TiNi-Ti<sub>2</sub>Ni intermetallic compound composite coating on the surface of a TA15 titanium alloy, with a Ti-Ni-B<sub>4</sub>C powder mixture as the raw material. The highest microhardness value of the coating was about 700 HV, which was about 2.07 times that of the matrix (340 HV), and the wear quality of the coating was only 0.47% of the matrix. Chen et al. [8] used laser cladding technology to clad TiN powder onto the surface of a TC9 titanium alloy to prepare a TiN coating. The results showed that the wear of the TiN coating under 10 kg and 30 kg loads was about 1/100 and 1/30 of the matrix, respectively, which indicates that the wear resistance of the coating greatly improved. Hu et al. [9] used a YAG laser to laser clad a Ti-based Cr<sub>2</sub>C<sub>3</sub> alloy powder onto the surface of a Ti600 alloy to prepare a functional gradient coating, with TiC as the enhanced phase, making the average friction coefficient and wear rate of the coating only 0.3–0.5 times that of the Ti600 matrix, indicating that the wear resistance of the coating significantly improved. Cheng et al. [10] used laser cladding technology to prepare a NiCr/TiAl coating on the surface of a Ti600 titanium alloy. Their experimental results showed that the average microhardness of the coating was 832 HV, and the wear rate of the coating at room temperature was 27% that of the substrate.

In short, the current research on improving the wear resistance of titanium alloys mainly focuses on the preparation of metal–alloy composite coatings and ceramic coatings using laser cladding technology, while few studies have been conducted on the preparation of high-entropy boride coatings using laser cladding technology [11]. However, high-entropy borides have attracted much attention due to their comprehensive properties, such as their high melting point, excellent mechanical properties, and high thermal stability. For example, high-entropy diborides are considered candidate materials for components such as the leading edge of supersonic aircraft and metal-melting crucibles [12,13]. Since 2015, high-entropy boride ceramics dominated by high-entropy diborides have been widely studied [14–17]. According to the mixing rule, the theoretical hardness of high-entropy ceramic materials should be the sum of that of the single-phase materials of each component, but the actual values are often higher, particularly in high-entropy boride ceramics [18]. For example, Gild et al. [14] reported that the hardnesses of the ceramic blocks for six high-entropy borides—(Ti<sub>0.2</sub>Zr<sub>0.2</sub>Nb<sub>0.2</sub>Ta<sub>0.2</sub>Hf<sub>0.2</sub>)B<sub>2</sub>, (Ti<sub>0.2</sub>Zr<sub>0.2</sub>Hf<sub>0.2</sub>Ta<sub>0.2</sub>Mo<sub>0.2</sub>)B<sub>2</sub>, (Ti<sub>0.2</sub>Zr<sub>0.2</sub>Nb<sub>0.2</sub>Hf<sub>0.2</sub>Mo<sub>0.2</sub>)B<sub>2</sub>, (Ti<sub>0.2</sub>Zr<sub>0.2</sub>Nb<sub>0.2</sub>Ta<sub>0.2</sub>Cr<sub>0.2</sub>)B<sub>2</sub>, (Ti<sub>0.2</sub>Zr<sub>0.2</sub>Nb<sub>0.2</sub>Ta<sub>0.2</sub>Mo<sub>0.2</sub>)B<sub>2</sub>, and (Ti<sub>0.2</sub>Hf<sub>0.2</sub>Nb<sub>0.2</sub>Ta<sub>0.2</sub>Mo<sub>0.2</sub>)B<sub>2</sub>—were higher than those obtained using the mixing rule at 17.5 GPa, 19.1 GPa, 21.9 GPa, 19.9 GPa/23.7 GPa, and 22.5 GPa, respectively.

In view of the abovementioned excellent hardness properties of high-entropy borides, laser cladding was used in this study to obtain a composite coating containing the high-entropy (Ti<sub>0.2</sub>Zr<sub>0.2</sub>Mo<sub>0.2</sub>Ta<sub>0.2</sub>Nb<sub>0.2</sub>)B<sub>2</sub> boride phase on a Ti60 alloy with the Ti, Zr, Mo, Ta, Nb, and B powders as the raw materials. The microstructure and dry sliding friction and wear behavior of the coating were studied to provide a basis for the application of Ti60 alloy in wear-resistant environments.

## 2. Materials and Methods

Ti60 alloy, with a size of 100 mm × 50 mm × 5 mm, was used, and its composition is shown in Table 1. The base material samples were ultrasonically cleaned using acetone, ethanol, and deionized water, in that order, and then dried in an electric temperature air-drying oven at 60 °C for 8 h. Ti, Zr, Mo, Ta, and Nb metal powders with purities of 99.9 wt.% and B metal powder with a purity of 99.99 wt.% were evenly mixed in a grinding machine, and then the mixed powder was pre-coated onto the surface of the Ti60 alloy with a 4 wt.% PVA solution as the binder. The powder layer thickness was preset to about 1.5 mm. The proportions of the different elements in the mixed powder are shown in Table 2.

**Table 1.** Chemical composition of the main components in the Ti60 alloy.

Element	Al	Sn	Zr	Mo	Nb	Ta	Si	C	Ti
Wt.%	5.0–6.3	3.0–5.0	2.5–7.0	0.2–1.5	0.2–1.0	0.2–3.0	0.2–0.55	0.01–0.09	Bal.

**Table 2.** The proportion of different elements in the mixed powder.

Element	Ti	Zr	Mo	Ta	Nb	B
Wt.%	7.76	14.80	15.49	29.35	15.07	17.53

Laser cladding was carried out on a Rayco RFL-C6000 fiber laser cladding system (Wuhan Rayco Fiber Laser Technology Co., LTD., Wuhan, China), and the cladding process was protected using argon gas. The laser power, spot diameter, scanning speed, laser spot overlap rate, argon purity, and argon flow rate were 2600 W, 4.5 mm, 8 mm/s, 30%, 99.99%, and 15 L/min, respectively. The laser cladding samples were cut into 9 mm × 9 mm × 5 mm pieces using the wire cutting method in preparation for XRD, SEM, and the wear test. The phase composition of the coating was analyzed using an X'Pert PRO X-ray meter (XRD) produced by PANalytical in Almelo, The Netherlands. The target material of the XRD test, starting position 2θ, ending position 2θ, step size 2θ, scanning type, and divergence slit size were Cu, 19.9999°, 89.9975°, 0.0131303°, continuous, and 0.76 mm, respectively. The morphology and composition of the coating before and after the wear test were observed using a JSM-7600F high resolution scanning electron microscope (SEM) produced by JEOL Corporation, Akishima, Japan, which was equipped with an energy spectrometer.

Before the microhardness test of the coating and matrix, the sample was polished first, and then the microhardness at the cross-section of the coating was tested using a DHV-1000 digital display Vickers microhardness tester produced by Dongguan Zhongte Precision Instrument Technology Co., LTD, Dongguan, China. The loading load and loading time of the microhardness test were 100 g and 15 s, respectively. The microhardness test was carried out from the top of the coating to the substrate, and the interval of microhardness test points was 0.15 mm. The volume ratio of the corrosion reagent used in the experiment was HF:HNO<sub>3</sub>:H<sub>2</sub>O = 1:1:3.

Dry friction and wear tests were carried out on Ecomet300/Automet300 equipment (Buehler Company, Lake Bluff, IL, USA). A specific schematic diagram of the dry friction and wear is shown in [5]. The rotary speed, applied load, dry sliding speed, dry sliding wear time, total wear distance, and abrasive material were 200 r/min, 45 N, 0.921 m/s, 5 min, 276.3 m, and 200# SiC sandpaper, respectively. A Swiss Mettler Toledo XS105 (Mettler Toledo Company, Zurich, Switzerland) Dual Range analytical balance with an accuracy of 0.1 mg was used to weigh the wear samples before and after wear.

## 3. Results

### 3.1. Microstructure

The XRD pattern of the laser cladding coating is shown in Figure 1. Figure 1 shows that the coating mainly consisted of seven phases: (Ti<sub>0.2</sub>Zr<sub>0.2</sub>Mo<sub>0.2</sub>Ta<sub>0.2</sub>Nb<sub>0.2</sub>)B<sub>2</sub>, ZrB<sub>2</sub> (JCPDS

96-151-0857), TiB (JCPDS 96-900-8947), TiZr (JCPDS 96-153-9806),  $\text{Ti}_{1.83}\text{Zr}_{0.17}$  (JCPDS 96-154-1223),  $\text{Ti}_{0.67}\text{Zr}_{0.67}\text{Nb}_{0.67}$  (JCPDS 96-153-7634), and  $\text{TiO}_2$  (JCPDS 96-900-4145). The appearance of the  $\text{TiO}_2$  phase may have been caused by oxygen being present in the air during the laser cladding process. The position of the diffraction peak in the  $(\text{Ti}_{0.2}\text{Zr}_{0.2}\text{Mo}_{0.2}\text{Ta}_{0.2}\text{Nb}_{0.2})\text{B}_2$  phase was the same as that reported in [19]. During the laser cladding process, the mixed powder layer and part of the Ti60 matrix melted due to the absorption of the laser energy. Then, in the laser melt pool, the surface tension and buoyancy generated by the uneven temperature distribution promoted the formation of laser melt pool convection, so that various chemical elements in the mixed powder layer and the chemical elements of the partially melted Ti60 matrix were fully mixed. Finally, various borides and intermetallic compounds were generated following an in situ reaction. The following reactions may occur in the laser melt pool:

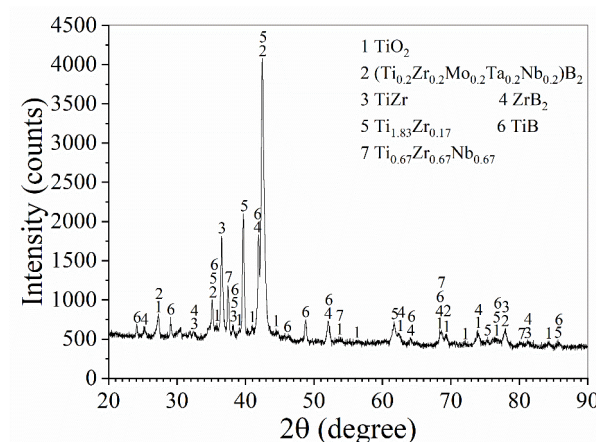
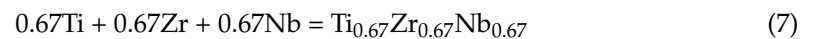
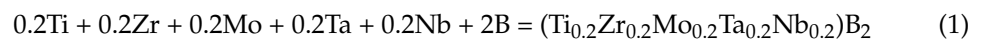


**Figure 1.** XRD pattern of the laser cladding coating.

Based on the strongest diffraction peak intensity of each phase, the XRD-K value method reported by Zheng et al. [20] was used in this study to calculate the semi-quantitative content of each phase in the coating. Detailed calculation formulas and methods can be found in [11]. In this study, the strongest diffraction peaks of  $\text{TiO}_2$ ,  $(\text{Ti}_{0.2}\text{Zr}_{0.2}\text{Mo}_{0.2}\text{Ta}_{0.2}\text{Nb}_{0.2})\text{B}_2$ ,  $\text{ZrB}_2$ ,  $\text{Ti}_{0.67}\text{Zr}_{0.67}\text{Nb}_{0.67}$ ,  $\text{TiB}$ ,  $\text{TiZr}$ , and  $\text{Ti}_{1.83}\text{Zr}_{0.17}$  were (110), (101), (011), (111), (101), and (101), respectively. The corresponding reference strength values (RIR values) were 3.5, 9.6, 9.32, 17.91, 1.85, 3.5, and 7.9, respectively. According to Formula (8) in [11], the mass fraction of each phase in the coating can be calculated as 3.4%, 34.17%, 6.18%, 3.75%, 36.19%, 6.20%, and 10.11%, respectively. That is to say,  $\text{TiB}$  and  $(\text{Ti}_{0.2}\text{Zr}_{0.2}\text{Mo}_{0.2}\text{Ta}_{0.2}\text{Nb}_{0.2})\text{B}_2$  are the two main generation phases.

The morphology of the whole laser cladding coating is shown in Figure 2, which demonstrates that the laser cladding coating was of good quality, and no obvious defects

such as pores and cracks were present in the coating. The interface between the coating and substrate was clear and well combined. The thickness of the coating was about 1.4–1.7 mm.

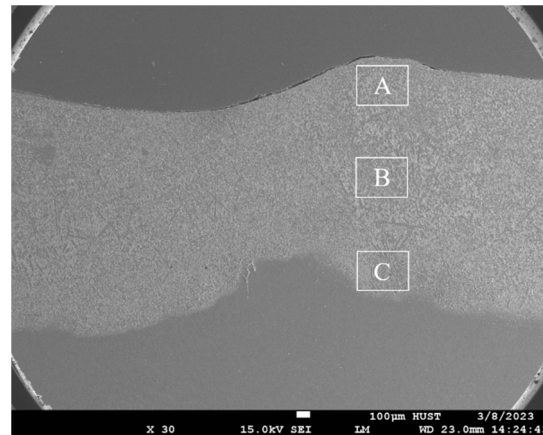


**Figure 2.** Morphology of a cross-section of the whole laser cladding coating. Where A represents the surface region of the coating, B represents the middle region of the coating, and C represents the interface region between the coating and substrate.

Enlarged images of the morphology of different regions in Figure 2 are shown in Figure 3, where Figure 3a–c show enlarged images of the morphology of surface region A, middle region B, and interface region C, respectively. Figure 3 shows that the morphology of the laser cladding coating mainly consists of whiskers or prisms. The reason why no significant differences were found in the morphology of different parts of the laser melt pool may be related to the homogenization of the convection mass transfer during the laser cladding process.

According to the EDS results in Table 3 and the XRD results in Figure 1, different phases in the laser cladding coating were roughly inferred to have formed via the following processes: firstly, via liquid solidification of the high-melting-point  $\text{ZrB}_2$  (melting point: 3250 °C) and  $(\text{Ti}_{0.2}\text{Zr}_{0.2}\text{Mo}_{0.2}\text{Ta}_{0.2}\text{Nb}_{0.2})\text{B}_2$  (melting point: 2966 °C) boride phases, and secondly, via solidification of the low-melting-point TiB (melting point: 2227 °C), TiZr,  $\text{Ti}_{1.83}\text{Zr}_{0.17}$ , and  $\text{Ti}_{0.67}\text{Zr}_{0.67}\text{Nb}_{0.67}$  phases after a decrease in the laser pool temperature following the residual liquid phase. The specific formation mechanism was studied in detail in the next step.

**Table 3.** EDS results at different positions in the laser cladding coating (at.%).

Position	Ti	Zr	Mo	Ta	Nb	B	Main Possible Phase
Spot 1	6.37	2.07	1.63	1.00	1.56	87.37	TiB + $(\text{Ti}_{0.2}\text{Zr}_{0.2}\text{Mo}_{0.2}\text{Ta}_{0.2}\text{Nb}_{0.2})\text{B}_2$
Spot 2	9.01	3.23	1.04	1.13	1.63	83.96	TiB + $(\text{Ti}_{0.2}\text{Zr}_{0.2}\text{Mo}_{0.2}\text{Ta}_{0.2}\text{Nb}_{0.2})\text{B}_2$
Spot 3	10.01	3.10	1.35	1.23	1.42	82.89	TiB + $(\text{Ti}_{0.2}\text{Zr}_{0.2}\text{Mo}_{0.2}\text{Ta}_{0.2}\text{Nb}_{0.2})\text{B}_2$
Spot 4	2.28	1.48	1.22	1.50	1.13	92.39	TiB + $(\text{Ti}_{0.2}\text{Zr}_{0.2}\text{Mo}_{0.2}\text{Ta}_{0.2}\text{Nb}_{0.2})\text{B}_2$
Spot 5	3.89	1.24	1.22	1.57	1.10	90.98	TiB + $(\text{Ti}_{0.2}\text{Zr}_{0.2}\text{Mo}_{0.2}\text{Ta}_{0.2}\text{Nb}_{0.2})\text{B}_2$
Spot 6	6.35	1.73	1.62	1.27	1.37	87.66	TiB + $(\text{Ti}_{0.2}\text{Zr}_{0.2}\text{Mo}_{0.2}\text{Ta}_{0.2}\text{Nb}_{0.2})\text{B}_2$
Spot 7	5.56	1.66	1.29	1.52	1.15	88.82	TiB + $(\text{Ti}_{0.2}\text{Zr}_{0.2}\text{Mo}_{0.2}\text{Ta}_{0.2}\text{Nb}_{0.2})\text{B}_2$
Spot 8	4.87	1.47	1.27	1.59	1.24	89.56	TiB + $(\text{Ti}_{0.2}\text{Zr}_{0.2}\text{Mo}_{0.2}\text{Ta}_{0.2}\text{Nb}_{0.2})\text{B}_2$
Spot 9	13.46	1.23	1.33	1.70	1.68	80.60	TiB + $(\text{Ti}_{0.2}\text{Zr}_{0.2}\text{Mo}_{0.2}\text{Ta}_{0.2}\text{Nb}_{0.2})\text{B}_2$
Spot 10	4.79	0.97	1.09	1.07	1.03	91.05	TiB + $(\text{Ti}_{0.2}\text{Zr}_{0.2}\text{Mo}_{0.2}\text{Ta}_{0.2}\text{Nb}_{0.2})\text{B}_2$



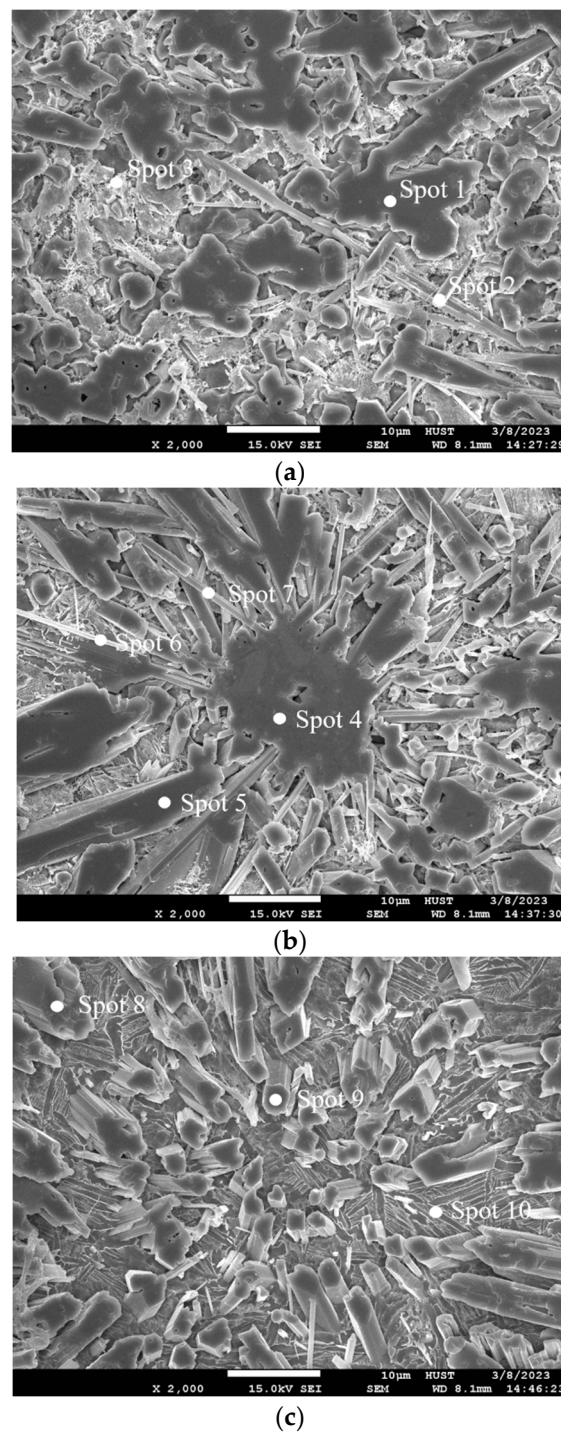


**Figure 3.** Enlarged images of the morphologies at different positions in Figure 2 for a cross-section of the laser cladding coating: (a) surface region A, (b) middle region B, and (c) interface region C.

The formation of the whisker or prismatic structure TiB in a laser cladding coating followed the following process: the B27 structure of TiB increased the growth rate in the [010] direction to be significantly faster than that in other directions, so whiskers or prismatic structures easily form [21], which can play roles in strengthening the substrate in the coating [22]. The structural morphology of TiB in Figure 3 is consistent with that reported in the literature [23,24]. In addition, because plane (001) of TiB grows the fastest and the remaining crystal faces, (100), (101), and (10 $\bar{1}$ ), make up the sides of TiB, the sectional whiskers or prismatic structures are mostly hexagonal [22]. When the temperature drops to

room temperature, the coating will eventually form a TiB mixed structure with whiskers or prismatic structures as the main body.

### 3.2. Wear Resistance Properties

The microhardness change curve for a cross-section of the laser cladding coating is shown in Figure 4, which shows that the microhardness of the laser cladding coating has a gradient trend, and the microhardness can be divided into a typical three-interval step distribution. The uneven distribution of the microhardness value of the coating was caused by the uneven distribution of the phases in the coating. The microhardness value of the coating surface was the highest (1287.8 HV<sub>0.1</sub>), with the microhardness value fluctuating slightly between 1287.8 and 1129.6 HV<sub>0.1</sub>. At 0.64 mm, a large decrease occurs, forming the second step, with a microhardness value between 905.3 and 824.2 HV<sub>0.1</sub>. Then, at 1.24 mm, a sharp drop characterizes the third step, with a microhardness value ranging from 420.5 to 356.6 HV<sub>0.1</sub>. We believe that the reasons for the variation in the hardness gradient of the coating are mainly correlated with the distribution and volume fraction of the phases with different proportions and hardnesses in the coating. This problem needs to be further studied in the future. Understanding the phase composition and volume fraction of different parts of the coating requires study of the temperature, flow, and mass fields of the coating via numerical simulations, and phase diagrams and rapid solidification theory should be used in combination with these results for further clarity. At present, we can only make a rough interpretation: the surface of the coating has a higher hardness, which decreases in the middle part and even further decreases near the interface. This is because only this distribution of high hardness phases may cause a gradient change in the studied coating. The minimum microhardness of the Ti60 matrix in this study was higher than that of the Ti60 matrix (340 HV) reported in [1]. That is, the microhardness of the coating fluctuated between 824.2 and 1287.8 HV<sub>0.1</sub>, and the average microhardness of the coating was about 1062.9 HV<sub>0.1</sub>, while the average microhardness of the Ti60 matrix was about 366.7 HV<sub>0.1</sub>. Thus, the average microhardness of the coating was about 2.9 times that of the Ti60 matrix. Three possible reasons can be proposed for the increase in microhardness of the laser cladding coating: First, the high-entropy boride phase and intermetallic compound phase in the coating are high-hardness phases (the hardness of (Ti<sub>0.2</sub>Zr<sub>0.2</sub>Mo<sub>0.2</sub>Ta<sub>0.2</sub>Nb<sub>0.2</sub>)B<sub>2</sub> is 23.7 GPa [14], the hardness of TiB is 35 GPa [25], and the hardness of ZrB<sub>2</sub> is 15.3 GPa [26]), and they are distributed in the coating to strengthen dispersion. Second, the coating contains a TiB phase with a nano-indentation hardness up to 35 GPa [25], and its whisker-like or prismatic structures play roles in strengthening the coating phase. Third, the laser cladding process is characterized by rapid heating and cooling, and the microstructure of the coating after laser cladding is fine, which thus results in fine crystal strengthening. In short, the increase in microhardness of the laser cladding coating will help to improve the wear resistance of the coating.

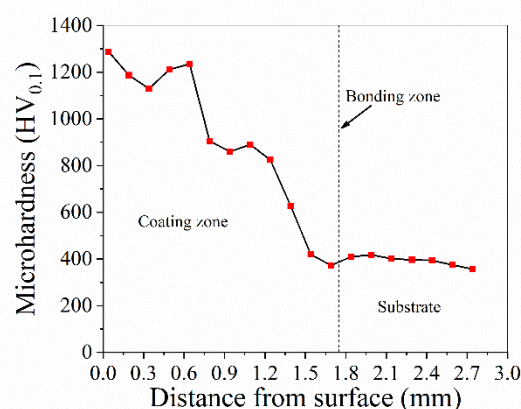
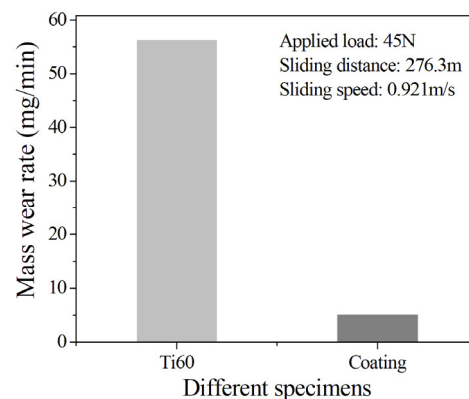


Figure 4. Microhardness curve for a cross-section of the laser coating.

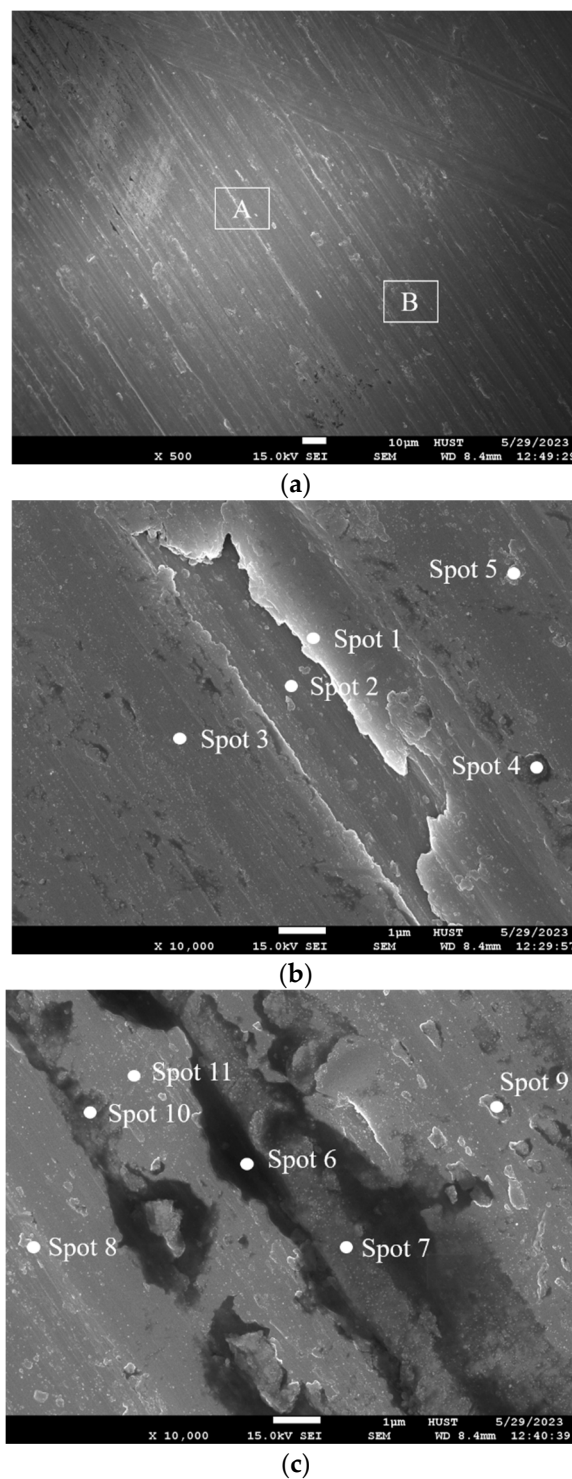
A columnar comparison of the mass wear rates of the coating and Ti60 substrate under dry friction and wear conditions at room temperature is shown in Figure 5. Figure 5 shows that under the same wear conditions, the mass wear rate of the coating was 5.14 mg/min, while that of the Ti60 substrate was 56.32 mg/min; that is, the wear resistance of the coating is significantly higher than that of the Ti60 alloy substrate, and the former was about 1/11 of the latter, which could be related to the high microhardness of the coating. In general, the greater the hardness of a material, the better its wear resistance [27]. Figure 4 shows that the average microhardness of the coating was 1062.9 HV<sub>0.1</sub>, which was about 2.9 times that of the Ti60 substrate, so the wear resistance of the coating significantly improved compared with that of the Ti60 substrate.



**Figure 5.** Columnar comparison of mass wear rates between the coating and Ti60 matrix.

Figure 6 shows the surface wear morphology of the Ti60 matrix after dry friction and wear. Figure 6 shows that the worn surface of the Ti60 substrate was severely scratched and presented many parallel furrows, which was a typical abrasive wear characteristic. The friction pair was pressed into the friction surface under normal load, and the sliding friction force caused the friction surface to shear, plow, and cut through the furrow action of the grinding pair, resulting in grooving wear marks. The number of furrows on the surface of the Ti60 matrix was large, the depth and width were large, metal debris accumulated at the edges of the wear marks, and serious plastic deformation occurred on the surface of the wear marks. This was due to the low hardness of the Ti60 matrix, at about 366.7 HV<sub>0.1</sub> (Figure 4), while the hardness value of the SiC particles in the grinding pair was as high as 3200 HV [28]. Therefore, during dry friction and wear, hard SiC particles have a strong ploughing effect on the surface of the Ti60 matrix, resulting in a large amount of wear. At the same time, under the repeated action of friction pairs, the materials cut off from the surface of the Ti60 matrix were compressed and adhered to the surface, leading to adhesive wear (Figure 6b,c). In addition, the EDS results in Table 4 show that the Ti60 matrix was oxidized due to heat generation during dry friction and wear. Therefore, the type of wear affecting the Ti60 matrix was a combination of abrasive, adhesive, and oxidation wear, but the proportion of abrasive wear was the largest.



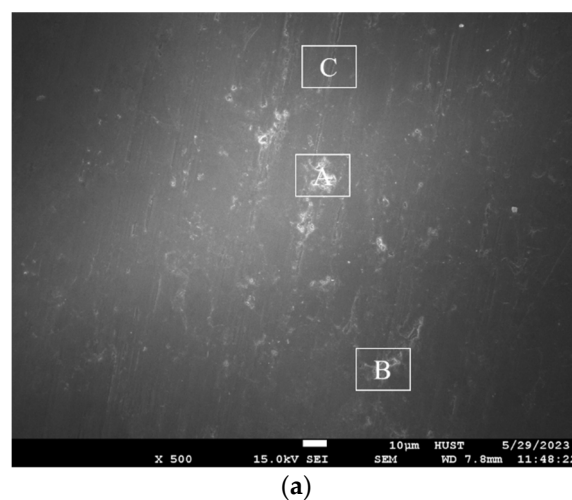


**Figure 6.** SEM image of the Ti60 matrix after wear: (a) whole worn surface, (b) enlarged SEM image at zone A in (a), and (c) enlarged SEM image at zone B in (a).

**Table 4.** EDS results of the Ti60 matrix's worn surface at different positions (at.%).

Element	Spot 1	Spot 2	Spot 3	Spot 4	Spot 5	Spot 6	Spot 7	Spot 8	Spot 9	Spot 10	Spot 11
Ti	68.99	69.83	68.78	58.93	70.01	58.00	65.09	65.07	54.94	65.71	61.82
Al	8.73	7.84	8.67	8.11	8.27	6.70	9.55	7.86	7.57	8.41	8.43
Zr	7.40	6.32	6.61	6.24	6.46	5.56	6.57	7.08	6.03	6.56	6.15
Mo	0.39	0.39	0.13	0.73	0.60	0.18	0.47	0.58	0.35	0.37	0.34
Ta	0.06	0.11	0.15	-	-	-	0.16	-	-	-	-
Nb	0.25	-	-	-	0.33	0.04	0.07	0.38	-	-	0.23
Si	0.53	0.80	0.74	0.90	0.64	0.40	0.69	0.54	0.52	0.91	0.74
Sn	1.38	1.16	1.35	1.22	1.33	1.18	1.20	1.24	0.94	1.28	1.18
O	12.27	13.55	13.57	23.87	12.36	27.94	16.20	17.25	29.65	16.76	21.11

The morphology of the worn surface of the coating after dry friction and wear is shown in Figure 7, which shows that the worn surface of the coating was relatively smooth, with shallow furrows and partial adhesion to the crushed area on the surface. This shows that the types of wear affecting the coating were abrasive and adhesive wear. At the same time, the material debris at the edge of the furrow accumulated in the furrow after repeated rolling, which hindered smooth formation of the furrow and improved the wear resistance of the coating. The size of the furrow on the coating surface was closely related to the microhardness of the coating. The abrasive dust accumulated on and adhered to the surface of the coating during repeated grinding of the friction pair, and the harder abrasive dust hindered complete formation of the furrow. The different sizes of the particles in the coating were related to the volume fraction of the different kinds of boride ceramic phases and intermetallic compound phases. In addition, the EDS results in Table 5 show that during dry friction and wear, the coating was oxidized due to the generation of friction heat. Therefore, the type of wear affecting the coating was actually a combination of abrasive, adhesive, and oxidation wear.

**Figure 7.** Cont.

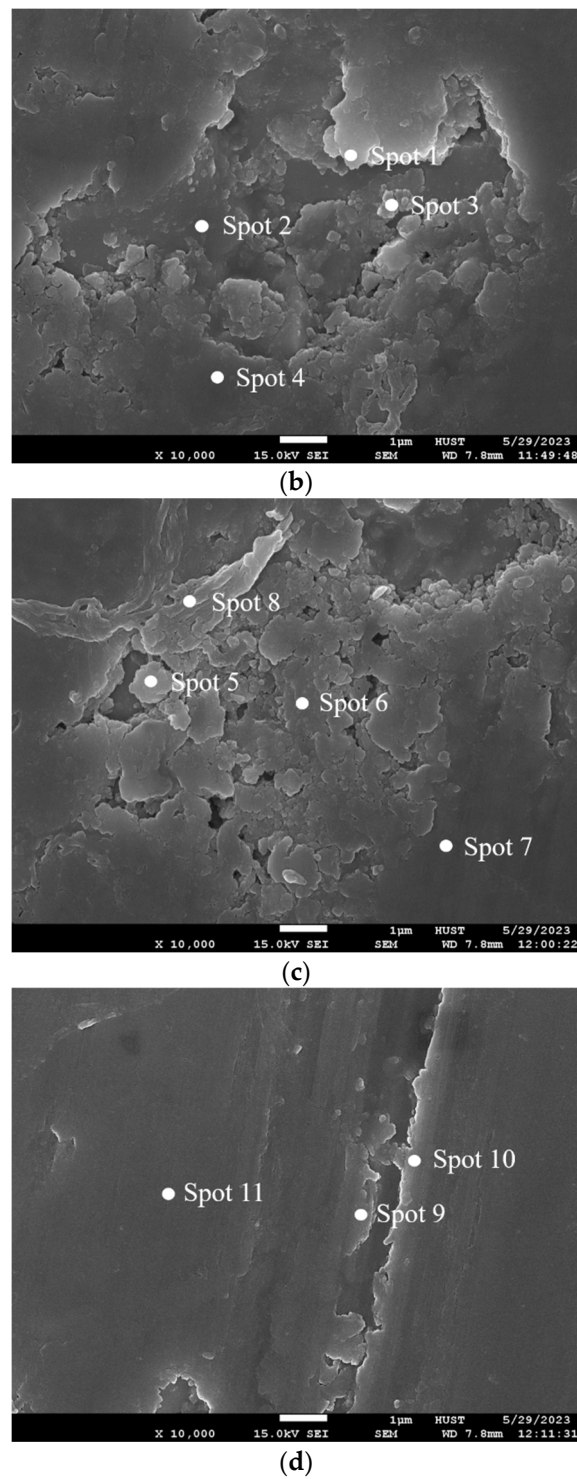


**Figure 7.** SEM image of coating after wear: (a) whole worn surface, (b) enlarged SEM image at zone A in (a), (c) enlarged SEM image at zone B in (a), and (d) enlarged SEM image at zone C in (a).

**Table 5.** EDS results of the coating's worn surface at different positions (at.%).

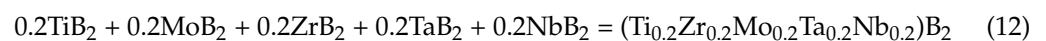
Element	Spot 1	Spot 2	Spot 3	Spot 4	Spot 5	Spot 6	Spot 7	Spot 8	Spot 9	Spot 10	Spot 11
Ti	11.97	12.41	21.75	10.92	7.73	8.7	8.07	8.89	13.46	10.26	15.86
Zr	3.18	2.36	4.52	2.15	2.14	2.82	2.33	2.2	2.86	2.47	2.52
Mo	1.24	0.89	1.83	0.72	1.13	0.87	1.11	0.98	1.77	1.93	1.78
Ta	0.79	2.03	1.87	1.58	0.64	0.99	0.66	1.23	0.38	0.27	1.23
Nb	0.57	1.08	1.59	0.96	0.66	0.66	0.4	0.68	0.85	0.72	0.87
B	68.29	71.82	53.58	75.16	74.6	69.7	75.89	76.59	69.34	71.73	67.99
O	13.96	9.41	14.86	8.51	13.1	16.26	11.54	9.43	11.34	12.62	9.75

In summary, the type of wear affecting the Ti60 matrix was mainly abrasive wear, accompanied by a small amount of adhesive and oxidative wear, while a combination of abrasive, adhesive, and oxidative wear affected the coating.

#### 4. Discussion

##### 4.1. Microstructure Formation Mechanism of the Coating

During the laser cladding process, a large temperature gradient forms inside and on the surface of the general laser melt pool. The surface tension and buoyancy generated by the uneven temperature distribution promote the formation of convection in the laser melt pool, so that various chemical elements in the mixed powder layer become fully mixed with those in the partially melted Ti60 matrix. The composition distribution of the cladding layer was macroscopically uniform, and an in situ reaction occurred to form high-entropy borides, diborides, TiB, and the intermetallic compound phases. In accordance with the in situ reaction formation mechanism of the laser cladding coating reported in [29], Figure 8 shows the formation process of different phases in the laser cladding pool of the coating. The formation process of each phase in the coating can be seen in Table 6 and Figure 8: under the action of a laser heat source, the Ti, Zr, Mo, Ta, Nb, and B powders of the preset powder layer melt to form a laser cladding pool, and TiB<sub>2</sub> and ZrB<sub>2</sub> single-component diborides were preferentially formed, which can be seen in Figures 1 and 9. At the same time, the transition metals Ti, Zr, Mo, Ta, and Nb react in situ with B elements to form the high-entropy (Ti<sub>0.2</sub>Zr<sub>0.2</sub>Mo<sub>0.2</sub>Ta<sub>0.2</sub>Nb<sub>0.2</sub>)B<sub>2</sub> boride phase. The TiB, TiZr, Ti<sub>1.83</sub>Zr<sub>0.17</sub>, and Ti<sub>0.67</sub>Zr<sub>0.67</sub>Nb<sub>0.67</sub> intermetallic compound phases were then subsequently formed. In addition, it should be pointed out that Reactions (9)–(12) in Figure 9 are as follows:

**Table 6.** Melting points and boiling points of different elements (K).

Element	Ti	Zr	Hf	Ta	Nb	Cr	Mo	B
Melting point	1941	2125	2506	3287	2750	2180	2896	2348
Boiling point	3560	4682	4876	5726	5017	2952	4912	4273

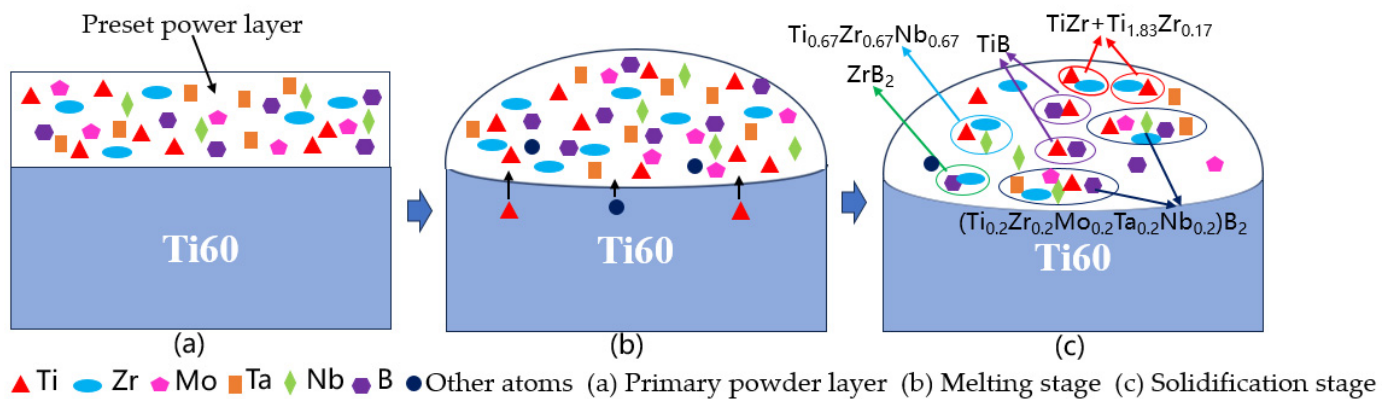


**Figure 8.** Schematic diagram of the different phase formation processes in the laser cladding pool of the coating.

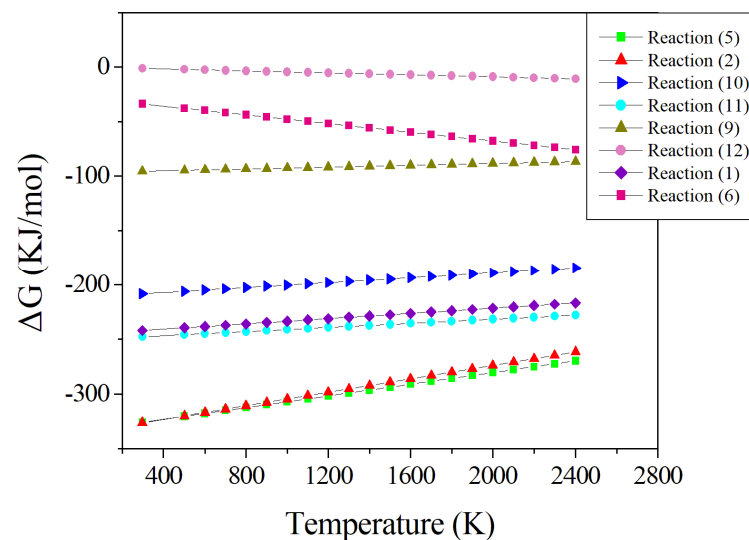


**Figure 9.** Gibbs free energy,  $\Delta G$ , curves of different reactions with temperature T.

#### 4.2. Wear Mechanism of the Coating and Ti60 Matrix

In the material friction and wear test, the amount of wear in the material is usually used to evaluate the wear resistance of the material. That is to say, the smaller the amount of wear loss per unit time or per unit friction distance, the better the wear resistance of the material. The wear mechanism of the material, under dry friction and wear conditions, generally involves three kinds of wear: adhesive wear, abrasive wear, and oxidation wear.

##### (1) Adhesive wear

According to the adhesive wear theoretical model proposed by world-renowned tribology expert Professor Archard in 1953 [30], hemispherical micro-convex bodies with multiple smooth surfaces are assumed to exist between the friction pair materials. When the micro-convex bodies come into contact, due to the action of local concentrated stress, plastic deformation occurs at the area of contact, which is relative to the amount of motion. The formula for calculating adhesive wear V is derived as follows:

$$V = K_1(NL/H) \quad (13)$$

where  $K_1$ , V, N, L, and H are the wear coefficient, adhesive wear amount, normal load, relative sliding distance, and material hardness, respectively.



From Formula (13), adhesive wear  $V$  can be seen to be proportional to friction sliding distance  $L$  and normal load  $N$  and is inversely proportional to the surface hardness  $H$  of the softer material. Therefore, under the same wear conditions, the amount of wear in the high-hardness materials is low and the wear resistance is good.

In the friction pairs presented in this study, the hardness of the abrasive SiC sandpaper (3200 HV [28]) is significantly higher than that of the coating and Ti60 matrix (Figure 4), indicating that both the coating and Ti60 matrix are suitable for the Archard model and consistent with the SEM morphology of the wear surface (Figures 6 and 7). Therefore, adhesive wear affects the coating and Ti60 matrix.

## (2) Abrasive wear

In the model proposed by Rabinowicz [31] for wear with abrasive particles, assuming that a conical rigid micro-convex body with radius  $r$  slides on the surface of the grinding material to form a furrow with depth  $x$ , the amount of wear  $V$  of the material per unit distance can be expressed as follows:

$$V = K_2(N/H) \quad (14)$$

where  $K_2$ ,  $N$ , and  $H$  are the wear coefficient, normal load, and hardness of the pressed material, respectively. From Formula (14), we can conclude that the higher the hardness of the material, the lower the wear amount.

In the friction pair composed of abrasive SiC sandpaper, the coating and Ti60 matrix in this study also conform to the Rabinowicz model and the SEM morphology of the wear surface (Figures 6 and 7); that is, the wear surface of the coating and Ti60 matrix have typical furrow characteristics. Therefore, abrasive wear also affects the coating and Ti60 matrix.

## (3) Oxidative wear

Under dry friction and wear conditions, the surface temperature increases due to heating, which leads to oxidation of the surface material. Since both the coating and Ti60 matrix experience dry friction wear, the generation of friction heat will become increasingly serious with an increase in wear over time, resulting in oxidation on the surface of the coating and Ti60 matrix, evidenced by the detection of O at each position in Tables 4 and 5.

In summary, the types of wear affecting the laser cladding coating and Ti60 substrate in this study were abrasive, adhesive, and oxidation wear in the friction pair composed of abrasive SiC sandpaper. However, the proportions of these three types of wear are different with different hardnesses of the coating or Ti60 matrix.

## 5. Conclusions

- (1) Laser cladding was successfully used to obtain a composite containing the high-entropy  $(\text{Ti}_{0.2}\text{Zr}_{0.2}\text{Mo}_{0.2}\text{Ta}_{0.2}\text{Nb}_{0.2})\text{B}_2$  boride phase at 34.17 wt.% to coat the Ti60 alloy. Ti, Zr, Mo, Ta, Nb, and B powders were used as the raw materials, and the bond between the coating and the substrate was strong.
- (2) The wear resistance of the laser cladding composite coating was greatly improved due to the occurrence of the high-hardness  $(\text{Ti}_{0.2}\text{Zr}_{0.2}\text{Mo}_{0.2}\text{Ta}_{0.2}\text{Nb}_{0.2})\text{B}_2$  phase, and the mass wear rate of the coating was about 1/11 that of the Ti60 substrate.
- (3) The main types of wear in the laser cladding composite coating were abrasive, adhesive, and oxidative wear, while that of the Ti60 matrix was mainly abrasive wear, accompanied by a small amount of adhesive and oxidative wear.

**Author Contributions:** Investigation, K.H. and X.H.; writing—original draft preparation, X.H.; writing—review and editing, K.H. All authors have read and agreed to the published version of the manuscript.

**Funding:** This work was supported by the Open Project Program (No. 23-1) of the Key Laboratory of Laser Technology and Optoelectronic Functional Materials of Hainan Province, Hainan Normal University.

**Institutional Review Board Statement:** Not applicable.

**Informed Consent Statement:** Not applicable.

**Data Availability Statement:** The data used in this study are available from the corresponding author upon reasonable request.

**Acknowledgments:** The authors are also grateful to the Analytical and Testing Center of Huazhong University of Science and Technology.

**Conflicts of Interest:** The authors declare no conflicts of interest.

## References

- Wang, S.H.; Xin, B.; Zhao, Q.Z.; Jiao, Y.X.; Qiang, W. Effect of heat treatment on microstructure and tensile properties of electron beam welded TC4/Ti60 joint. *Electr. Weld. Mach.* **2020**, *50*, 16–20.
- Di, Y.N.; Liu, H.X.; Zhang, X.W.; Chen, L.; Liu, J.Z.; Lin, J.Q.; Hao, X.H.; Wang, Y.Y. Friction and wear behavior and high-temperature oxidation resistance of laser cladding AlCoCrFeMoVTi high-entropy alloy coating on titanium alloy surface. *Rare Met. Mat. Eng.* **2021**, *50*, 2883–2891.
- Qin, X.; Qi, W.J.; Zuo, X.G. Friction and high temperature oxidation resistance of laser cladding NiCrCoAlY-Cr<sub>3</sub>C<sub>2</sub> composite coating on TC4 titanium alloy. *J. Mater. Eng.* **2021**, *49*, 107–114.
- Jiang, C.P.; Zhang, J.; Chen, Y.N.; Hou, Z.M.; Zhao, Q.Y.; Li, Y.; Zhu, L.X.; Zhang, F.Y.; Zhao, Y.Q. On enhancing wear resistance of titanium alloys by laser clad WC-Co composite coatings. *Int. J. Refract. Met. Hard Mater.* **2022**, *107*, 105902. [\[CrossRef\]](#)
- Huang, K.J.; Huang, W.X. Microstructure and wear resistance of Ti<sub>5</sub>Si<sub>3</sub>/Ti<sub>3</sub>Al composite coatings prepared by laser cladding on TA2 titanium alloy. *Lubricants* **2023**, *11*, 213. [\[CrossRef\]](#)
- Yu, J.J.; Zhang, X.Y.; Ma, L.L.; Li, H.; Zou, L.J.; Zhang, W.P. Microstructures and properties of laser cladding Ti/Ni+Si<sub>3</sub>N<sub>4</sub>/ZrO<sub>2</sub> composite coatings on TA15 titanium alloys. *Surf. Technol.* **2016**, *45*, 105–109.
- Feng, S.R.; Tang, H.B.; Zhang, S.Q.; Wang, H.M. Microstructure and wear resistance of laser clad TiB-TiC/TiNi-Ti<sub>2</sub>Ni intermetallic coating on titanium alloy. *Trans. Nonferrous Met. Soc. China* **2012**, *22*, 1667–1673. [\[CrossRef\]](#)
- Chen, C.N.; Su, M. Study on microstructure and abrasive resistance of laser cladding TiN surface alloyed TC9. *Beijing Univ. Aeronaut. Astronaut. J.* **1998**, *24*, 253–255.
- Hu, F.Y.; Cui, A.Y.; Hui, L.; Peng, X. Wear and corrosion behavior of Ti-matrix functional gradient layer. *J. Funct. Mater.* **2012**, *43*, 36–38.
- Cheng, C.X.; Li, Y.F.; Liu, S.D. Surface modification of Ti600 Ti-alloy with laser clad NiCr/TiAl coating. *Chin. J. Vac. Sci. Technol.* **2020**, *40*, 1166–1170.
- Huang, K.J.; Han, X.C. High-temperature oxidation properties of Ti-Hf-Mo-Ta-Nb-B composite coating deposited on Ti60 alloy with laser cladding. *Coatings* **2023**, *13*, 1646. [\[CrossRef\]](#)
- Fahrenholtz, W.G.; Hilmas, G.E. Ultra-high temperature ceramics: Materials for extreme environments. *Scr. Mater.* **2017**, *129*, 94–99. [\[CrossRef\]](#)
- Weinberger, C.R.; Thompson, G.B. Review of phase stability in the group IVB and VB transition-metal carbides. *J. Am. Ceram. Soc.* **2018**, *101*, 4401–4424. [\[CrossRef\]](#)
- Gild, J.; Zhang, Y.Y.; Harrington, T.; Jiang, S.C.; Hu, T.; Quinn, M.C.; Mellor, W.M.; Zhou, N.X.; Vecchio, K.; Luo, J. High-entropy metal diborides: A new class of high-entropy materials and a new type of ultrahigh temperature ceramics. *Sci. Rep.* **2016**, *6*, 37946. [\[CrossRef\]](#) [\[PubMed\]](#)
- Gu, J.F.; Zou, J.; Sun, S.K.; Wang, H.; Yu, S.Y.; Zhang, J.Y.; Wang, W.M.; Fu, Z.Y. Dense and pure high-entropy metal diboride ceramics sintered from self-synthesized powders via boro/carbothermal reduction approach. *Sci. China Mater.* **2019**, *62*, 1898–1909. [\[CrossRef\]](#)
- Gild, J.; Wright, A.; Quiambao-Tomko, K.; Qin, M.D.; Tomko, J.A.; Shafkat bin Hoque, M. Thermal conductivity and hardness of three single-phase high-entropy metal diborides fabricated by borocarbothermal reduction and spark plasma sintering. *Ceram. Int.* **2020**, *46*, 6906–6913. [\[CrossRef\]](#)
- Zhang, Y.; Jiang, Z.B.; Sun, S.K.; Guo, W.M.; Chen, Q.S.; Qiu, J.X.; Plucknett, K.; Lin, H.T. Microstructure and mechanical properties of high-entropy borides derived from boro/carbothermal reduction. *J. Eur. Ceram. Soc.* **2019**, *39*, 3920–3924. [\[CrossRef\]](#)
- Zhao, P.B.; Zhang, Y.; Zhu, J.P.; Xu, L.; Zhou, Y.Z.; Guo, W.M.; Zhang, G.J.; Wang, H.L.; Lin, H.T. Research progress on high-entropy boride ceramics. *J. Chin. Ceram. Soc.* **2022**, *50*, 1512–1526.
- Barbarossa, S.; Orrù, R.; Cannillo, V.; Iacomini, A.; Garroni, S.; Murgia, M.; Cao, G. Fabrication and characterization of quinary high entropy-ultra-high temperature diborides. *Ceramics* **2021**, *4*, 108–120. [\[CrossRef\]](#)
- Zheng, Q.; Wang, X.H.; Xing, J.J.; Gu, H.; Zhang, G.J. Quantitative analysis for phase compositions of ZrB<sub>2</sub>-SiC-ZrC ultra-high temperature ceramic composites. *J. Inorg. Mater.* **2013**, *28*, 358–362. [\[CrossRef\]](#)
- Li, L.; Yu, Z.S.; Wang, H.P.; Li, M.P. Microstructural evolution of titanium substrate composite coatings reinforced by in situ synthesized TiB and TiC by laser cladding. *Int. J. Miner. Metall. Mater.* **2010**, *17*, 481–488. [\[CrossRef\]](#)
- He, B.; Lan, J.J.; Yang, G.; Wei, H. Microstructure and wear-resistant properties of in situ TiB-TiC reinforced titanium matrix composites by laser deposition manufacturing. *Rare Met. Mat. Eng.* **2017**, *46*, 3805–3810.

23. Lu, W.J.; Wu, R.J.; Zhang, D.; Zhang, X.N.; Sakata, T.; Mori, H. Interfacial microstructure of TiB/Ti in a Ti-TiB-TiC in situ composite. *Compos. Interface* **2002**, *9*, 41–50. [[CrossRef](#)]
24. Feng, H.B.; Zhou, Y.D.; Jia, C.; Meng, Q.C.; Rao, J.C. Growth mechanism of in situ TiB whiskers in spark plasma sintered TiB/Ti metal substrate composites. *Cryst. Growth Des.* **2006**, *6*, 1626–1630. [[CrossRef](#)]
25. Zhang, M.Q.; Yu, H.L.; Wang, H.M.; Yin, Y.L.; Wei, M.; Qiao, Y.L.; Zhang, W.; Xu, B.S. Microstructure and mechanical properties of in-situ TiB reinforced Ti-based composite coating by induction cladding. *J. Mater. Eng.* **2020**, *48*, 111–118.
26. Chamberlain, A.L.; Fahrenholtz, W.G.; Hilmas, G.E.; Ellerby, D.T. High-strength zirconium diboride-based ceramics. *J. Am. Ceram. Soc.* **2004**, *87*, 1170–1172. [[CrossRef](#)]
27. Li, X.Y.; Shao, H.H.; Zhang, B.S.; Dong, Q.S.; Li, C.L. High-temperature tribological properties of plasma sprayed Al<sub>2</sub>O<sub>3</sub>-13% TiO<sub>2</sub> coatings with microstructured and nanostructured feedstocks. *Mater. Prot.* **2019**, *52*, 1–7.
28. Zhang, H.X. Investigation on Microstructure and Wear Resistance of Ti-Al-Si Ceramic Composite Coatings on Titanium Alloys by Laser Cladding. Doctoral Thesis, Shandong University, Jinan, China, 23 May 2016.
29. Yang, L.Q.; Li, Z.Y.; Zhang, Y.Q.; Wei, S.Z.; Wang, Y.J.; Kang, Y. In-situ TiC-Al<sub>3</sub>Ti reinforced Al-Mg composites with Y<sub>2</sub>O<sub>3</sub> addition formed by laser cladding on AZ91D. *Surf. Coat. Technol.* **2020**, *383*, 125249. [[CrossRef](#)]
30. Archard, J.F. Contact and rubbing of flat surfaces. *J. Appl. Phys.* **1953**, *24*, 981–988. [[CrossRef](#)]
31. Rabinowicz, E.; Mutis, A. Effect of abrasive particle size on wear. *Wear* **1965**, *8*, 381–390. [[CrossRef](#)]

**Disclaimer/Publisher’s Note:** The statements, opinions and data contained in all publications are solely those of the individual author(s) and contributor(s) and not of MDPI and/or the editor(s). MDPI and/or the editor(s) disclaim responsibility for any injury to people or property resulting from any ideas, methods, instructions or products referred to in the content.